Phase transitions and equation of state of forsterite to 90 GPa from single-crystal X-ray diffraction and molecular modeling

GREGORY J. FINKELSTEIN[1,*], PRZEMYSLAW K. DERA[2,3], SANDRO JAHN[4], ARTEM R. OGANOV[5], CHRISTOPHER M. HOLL[1], YUE MENG[6] AND THOMAS S. DUFFY[1]

[1]Department of Geosciences, Princeton University, Princeton, New Jersey 08544, U.S.A.
[2]GSECARS, University of Chicago, Building 434A, 9700 South Cass Avenue, Argonne, Illinois 60439, U.S.A.
[3]Hawaii Institute of Geophysics and Planetology, School of Ocean and Earth Science and Technology, University of Hawaii, 1680 East West Road (POST Bldg 819E), Honolulu, Hawaii 96822, U.S.A.
[4]GFZ German Research Centre for Geosciences, Telegrafenberg, 14473 Potsdam, Germany
[5]Department of Geosciences and Department of Physics and Astronomy, Stony Brook University, Stony Brook, New York 11794, U.S.A.
[6]HPCAT, Carnegie Institution of Washington, Building 434E, 9700 South Cass Avenue, Argonne, Illinois 60439, U.S.A.

ABSTRACT

Forsterite, Mg_2SiO_4, the magnesian end-member of the olivine system, is the archetypal example of an orthosilicate structure. We have conducted synchrotron-based single-crystal X-ray diffraction experiments to 90 GPa on synthetic end-member forsterite to study its equation of state and phase transitions. Upon room-temperature compression, the forsterite structure is observed to 48 GPa. By fitting a third-order Birch-Murnaghan equation of state to our compression data, we obtain the zero-pressure isothermal bulk modulus, $K_{0T} = 130.0(9)$ GPa and its pressure derivative, $K'_{0T} = 4.12(7)$ for a fixed room-pressure volume, $V_0 = 290.1(1)$ Å^3, in good agreement with earlier work. At 50 GPa, a phase transition to a new structure (forsterite II) occurs, followed by a second transition to forsterite III at 58 GPa. Forsterite III undergoes no additional phase transitions until at least 90 GPa. There is an ~4.8% volume reduction between forsterite and forsterite II, and a further ~4.2% volume reduction between forsterite II and III. On decompression forsterite III remains until as low as 12 GPa, but becomes amorphous at ambient conditions. Using our X-ray diffraction data together with an evolutionary crystal structure prediction algorithm and metadynamics simulations, we find that forsterite II has triclinic space group $P1$ and forsterite III has orthorhombic space group $Cmc2_1$. Both high-pressure phases are metastable. Metadynamics simulations show a stepwise phase transition sequence from 4-coordinated Si in forsterite to mixed tetrahedral and octahedral Si (as in forsterite II), and then fully sixfold-coordinated Si (as in forsterite III), occurring by displacement in [001](100). The forsterite III structure is a member of the family of post-spinel structures adopted by compositions such as $CaFe_2O_4$ and $CaTi_2O_4$.

Keywords: Compressibility measurements, olivine, forsterite composition, single-crystal XRD data, synchrotron source, high-pressure olivine phase transition, diamond-anvil cell

INTRODUCTION

There are few minerals comparable to olivine, $(Mg,Fe)_2SiO_4$, in overall importance. On Earth, olivine occurs widely in igneous and metamorphic rocks (Deer et al. 1982) and is the dominant mineral phase of Earth's upper mantle (Ringwood 1991). It is also found in meteorites (Mason 1963), comets (Crovisier et al. 1997; Zolensky et al. 2006), pre-solar grains (Nguyen and Zinner 2004), other planets (Mustard et al. 2005), and in accretion disks around young stars (van Boekel et al. 2004). In the Earth's upper mantle, phase transitions in Mg-rich olivine and its polymorphs are believed to be responsible for the major seismic discontinuities at 410, 520, and 660 km depth (Ringwood 1991). Olivine's creep behavior exerts a major control on mantle rheology and affects the interpretation of seismic anisotropy (Karato and Wu 1993). While olivine transforms to wadsleyite at a depth near 410 km (~14 GPa) at normal mantle temperatures, it may persist metastably in cold subducting lithosphere below 410 km depth

and play a role in deep earthquake generation (Kirby et al. 1996; Kawakatsu and Yoshioka 2011). There has also been interest in the behavior of amorphous and liquid Mg_2SiO_4 over a wide range of pressures as a model system for understanding partial melting of the mantle, production of basalts and komatiites, and the behavior of magma oceans (Durben et al. 1993; de Koker et al. 2008; Adjaoud et al. 2011).

The structure of olivine ($Pbnm$, $Z = 4$) can be described as an expanded and distorted hexagonally close-packed (hcp) array of oxygen anions stacked along the **a** direction (Bragg and Brown 1926; Smyth et al. 2000). Si cations are located in tetrahedral sites, and Mg is in two distinct octahedral sites, one of which (M2) is larger and more distorted than the other (M1). Si-O tetrahedra are isolated and share corners with Mg-O octahedra, while the Mg-O octahedra share both corners and edges. There are three distinct oxygen sites: O1 and O2 are located on a mirror plane, while O3 is in a general position. Each oxygen anion is bonded to three octahedral cations and one tetrahedral cation. The addition of Fe slightly expands the unit cell and increases its distortion (Birle et al. 1968).

---

*E-mail: gjfinkel@princeton.edu

There is considerable controversy over the 300 K compression behavior in the olivine system. Above ~14 GPa, forsterite becomes metastable under 300 K compression. Previous studies report evidence for amorphization (Guyot and Reynard 1992; Durben et al. 1993; Andrault et al. 1995), a change in compression mechanism (Andrault et al. 1995; Rouquette et al. 2008), and a spin transition (Rouquette et al. 2008) with strong Fe-Mg compositional effects (Andrault et al. 1995) at high pressures. Whereas non-hydrostatic powder X-ray diffraction has been collected on forsterite up to 70 GPa (Andrault et al. 1995), single-crystal diffraction data have been reported only to 17 GPa (Downs et al. 1996). Due to the limitations of powder X-ray diffraction and spectroscopic studies, previous work has not been able to determine convincingly whether forsterite goes through a phase transition, amorphization, or a change in compression mechanism.

Single-crystal studies using laboratory-based X-ray sources have yielded important information on the equation of state and crystal structure variation of mantle minerals (Hazen and Finger 1982; Miletich et al. 2000). However, experiments with lab-based X-ray sources are generally limited to a maximum pressure of ~15 GPa. Recent advances in high-pressure single-crystal diffraction techniques using synchrotron sources (Dera et al. 2009, 2011a, 2011b; Dubrovinsky et al. 2010; Lavina et al. 2010, 2011; Kantor et al. 2012; Merlini et al. 2012) allow for the use of smaller and thinner crystals (~5–10 μm), which can be compressed to pressures approaching 1 megabar while retaining a quasi-hydrostatic stress environment. Single-crystal X-ray diffraction is particularly useful for investigating low-symmetry materials such as olivine. It eliminates the peak overlaps prevalent in powder diffraction and yields reliable peak intensities, allowing for the extraction of precise lattice constants and structural parameters. In this study, we have used single-crystal diffraction in conjunction with molecular modeling to investigate the compression of forsterite to 90 GPa and identify two new phase transitions to metastable structures.

METHOD

A synthetic crystal of forsterite, Mg_2SiO_4, was used. The sample was characterized at ambient conditions by X-ray diffraction, microprobe analysis, and Raman spectroscopy. No impurities at detectable levels were identified. The unit-cell parameters at ambient pressure are $a = 4.7543(5)$, $b = 10.201(2)$, and $c = 5.9819(8)$ Å, in good agreement with literature values (Smyth and McCormick 1995). Small crystals were polished to ≤7 μm thickness and pre-screened by synchrotron X-ray diffraction at beamline 13-BM-C of the GSECARS sector of the Advanced Photon Source (APS), Argonne National Laboratory. Crystals with sharp, circular diffraction peaks and off-axis crystal orientations were selected for further study.

High-pressure X-ray diffraction experiments were performed at the 16-ID-B beamline of the HPCAT sector and 13-BM-D of the GSECARS sector of the APS. Pressure was generated using a symmetric-type diamond-anvil cell with 200 μm diameter culets. The sample chamber was formed by drilling a ~110 μm hole in a rhenium gasket that had been pre-indented to ~30 μm thickness. Three 10×10 μm forsterite crystals were loaded into the sample chamber (Fig. 1). An annealed ruby ball and a ~10 μm gold foil were also included for pressure calibration (Fei et al. 2007). Pressures were calculated using the gold (111) peak due to its relative insensitivity to differential stress (Takemura and Dewaele 2008). To achieve quasi-hydrostatic conditions, the cell was loaded with a helium pressure-transmitting medium using the GSECARS/COMPRES gas-loading system. Rare gas solids such as helium provide optimum quasi-hydrostatic conditions at high pressures (Angel et al. 2007). An X-ray transparent cubic boron nitride (cBN) backing plate (seat) was used on the upstream diamond, while a tungsten carbide (WC) seat with a 60° opening-angle was used as the downstream seat.

Monochromatic diffraction experiments were performed at HPCAT using X-rays with a wavelength of 0.3989 Å and at GSECARS with a wavelength of
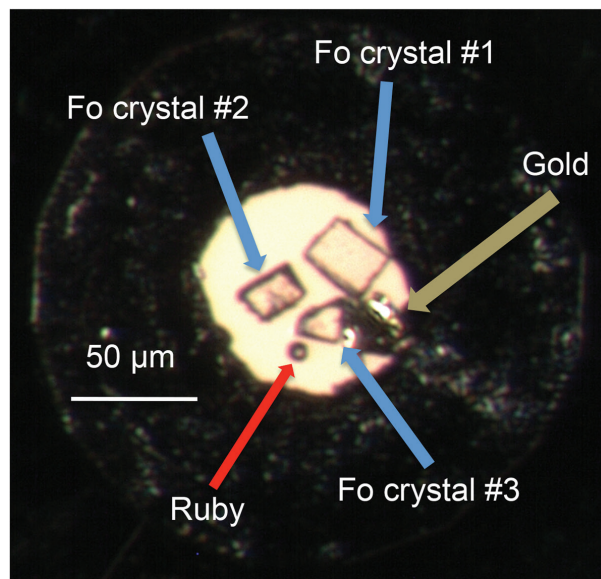

FIGURE 1. Sample configuration showing three forsterite crystals, a ruby ball, and a gold foil contained in a helium pressure-transmitting medium in a diamond-anvil cell.

0.3344 Å. Diffraction patterns were collected using a Mar CCD detector that was calibrated with a CeO_2 standard using the program FIT2D (Hammersley et al. 1996). The forsterite crystals were compressed in ~3–6 GPa steps using a gas-membrane drive. At each pressure, a wide ω scan was collected for each crystal, and at selected pressures, a stepped ω scan was carried out. The ω rotation is about the vertical axis of the diffractometer. Wide scans consisted of a 48° rotation of the diamond cell in ω while the detector was exposed. These were used to extract d-spacings, azimuthal angles around the beam center, and peak intensities. Step scans consisted of individual exposures taken at 1° intervals to constrain the ω angle of maximum intensity for each peak. This provides the third spatial coordinate necessary for reconstructing the crystal's reciprocal lattice, which is used to index the diffraction pattern. Wide scans and step scans were taken at the central detector position, as well as at lateral detector positions shifted ±70 mm to increase spatial coverage.

Peak fitting was performed using the program GSE_ADA (Dera et al. 2009). Polarization, Lorentz, and empirically determined diamond absorption corrections were applied to the fit peaks. The reciprocal lattices for each crystal were reconstructed using the software RSV (Dera et al. 2009). The unit cell and orientation matrix was found in RSV for each crystal by comparing combinations of reciprocal lattice point difference vectors. Twin domain orientations were identified using the program CELL_NOW (Bruker AXS Inc.). Transformations to conventional unit cells were determined using XPREP (Sheldrick 2008), and lattice parameters were refined in RSV using a least-squares fitting procedure. Crystal structures at selected pressures were refined in SHELX-97 (Sheldrick 2008).

To find the crystal structure of forsterite III, we resorted to simulation, using experimental unit-cell parameters as constraints in a global structure optimization using the evolutionary algorithm USPEX (Glass et al. 2006; Oganov and Glass 2006; Oganov et al. 2011; Lyakhov et al. 2013). This method searches for the global minimum of the relevant thermodynamic potential and has led to the discovery of new materials, including mineral phases (Oganov et al. 2006, 2009, 2010; Ma et al. 2009). We conducted searches at fixed volume and $T = 0$ K, and the relevant thermodynamic potential to be minimized was the internal energy. We conducted several searches, both with experimental cell parameters (with 28 atoms/cell), and with the same cell doubled in the **c**-direction (with 56 atoms/cell). In these searches, each generation consisted of 40 structures. A random symmetric algorithm using all orthorhombic space groups produced the first generation and 30% of each subsequent generation (Zhu et al. 2012; Lyakhov et al. 2013). Another 30% of each new generation were produced by heredity, 30% by softmutation (Lyakhov et al. 2010), and 10% by Mg-Si atomic permutation. All structures were relaxed within the fixed unit cell. For structure relaxations and energy calculations we used the GULP code (Gale 2005) and ionic shell model with previously published parameters (Catlow 1977; Sanders et al. 1984; Lewis and Catlow 1985). These

structure searches found the optimum structure with great efficiency, in ~30 min on a single-core PC. The four lowest-energy structures were selected and relaxed (both with fixed cell and with full relaxation) using ab initio calculations.

Phase transition mechanisms for high-pressure phases were explored by metadynamics in conjunction with classical molecular dynamics (MD) simulations. The simulation box contained 672 ions, which corresponds to a 4 × 2 × 3 supercell of the initial forsterite structure. First, this cell was equilibrated by molecular dynamics at $P = 50$ GPa and $T = 1000$ K in the *NPT* ensemble, i.e., at constant pressure and temperature. Particle interactions were modeled using an advanced ionic potential (Jahn and Madden 2007) that has been shown to be accurate for a wide range of pressures and temperatures, and was used successfully in previous studies of $MgSiO_3$ high-pressure phases (Jahn and Martoňák 2008; Haigis et al. 2012) and forsterite grain and phase boundary structures (Gurmani et al. 2011; Adjaoud et al. 2012). A Nosé-Hoover thermostat coupled to a barostat controlled temperature and pressure (Martyna et al. 1994). For the numerical integration of the equations of motion, a time step of 1 femtosecond was used.

As the experimentally observed phase transitions do not occur spontaneously during an MD simulation, metadynamics was used to force the system into a different state. In the present case, an algorithm described in Martoňák et al. (2006) was used that employs the components of the scaled simulation cell matrix as collective variables. The scaled coordinates were defined using the Hessian matrix calculated from the initial configuration that came from the MD simulation. A Gaussian height of 8.32 eV and a Gaussian width of 2.88 $eV^{1/2}$ were used as metadynamics parameters. In each metadynamics step, a short MD simulation of 1 ps was performed to relax the atomic positions and to obtain an average stress tensor for the respective configuration. In total, 1000 metadynamics steps were performed. This is the same approach used by Jahn and Martoňák (2008) to study phase transitions in orthoenstatite.

Lowest-energy structures from both global structure optimization and metadynamics were selected and relaxed using ab initio calculations in the framework of density functional theory (DFT) using the planewave code ABINIT (Gonze et al. 2009). The planewave basis set was expanded to 1000 eV and optimized norm-conserving pseudopotentials were used (Rappe et al. 1990). The exchange-correlation functional was treated in the generalized gradient approximation (Perdew et al. 1996). Appropriate k-point grids optimized by ABINIT were chosen to sample the Brillouin zones of the different unit cells. For each structure, full optimization was performed at a given target pressure, which includes atomic positions and unit-cell parameters.

RESULTS AND DISCUSSION

The measured X-ray diffraction patterns were consistent with the olivine structure to 48 GPa, indicating that at 300 K forsterite can persist metastably at pressures well above the ~14 GPa transition to the wadsleyite structure observed under high-temperature conditions. Results from a representative structure refinement of forsterite are shown in Table 1. At 50 GPa, an abrupt change in the diffraction pattern was observed (Fig. 2), indicating the presence of a new phase (designated as forsterite II). Slight variations were observed in the transition pressure across the three crystals in the cell as a result of a small pressure gradient. The crystals were preserved across the transition, but the high-pressure phase was twinned, necessitating the application of twin laws to index all the diffraction peaks. At 58 GPa, the diffraction pattern changed again indicating the formation of a second high-pressure phase (forsterite III). Unlike forsterite II, this phase is untwinned. This sequence of twinning among the phases is likely controlled by symmetry changes between each structure. The diffraction peaks from forsterite III show significant diffuse scattering, indicative of a high density of defects in the crystal. In addition, some extra peaks are visible adjacent to the main diffraction peaks that could be related to residual twin domains, but cannot be indexed due to their proximity to the main diffraction peaks (Fig. 2). Forsterite III was observed to 90 GPa, at which point diamond failure ended the experiment. The sequence of phase transitions, twinning, and diffuse scattering

TABLE 1a. Representative single-crystal structure refinement for forsterite at 45.3 GPa

Beamline	16 ID-B, HPCAT, APS, ANL
Wavelength (Å)	0.39891
Pressure (GPa)	45.3
Temperature (K)	298
Composition	Mg_2SiO_4
Symmetry	Orthorhombic, *Pbnm* (*Pnma*)
Lattice parameters a, b, c, (Å)	4.5232(5), 9.274(5), 5.5467(7)
Volume (Å)	232.7(2)
Z	4
R_{int}	0.072
Reflection range	$-5 \leq h \leq 5, -5 \leq k \leq 6, -7 \leq l \leq 7$
Maximum 2θ (°)	28.8
Number independent reflections	124
Refinement	F^2
R	0.048
wR_2	0.109

TABLE 1b. Refined atomic parameters for forsterite at 45.3 GPa

Atom	Wyckoff position	x/a	y/b	z/c	U_{iso}
Mg1	4a	0	0	0	0.0070(7)
Mg2	4c	0.9845(5)	0.2742(6)	0.25	0.0075(7)
Si	4c	0.4250(5)	0.0964(5)	0.25	0.0070(7)
O1	4c	0.7675(12)	0.0899(10)	0.25	0.0075(13)
O2	4c	0.2271(12)	0.4407(10)	0.25	0.0061(13)
O3	8d	0.2638(8)	0.1692(7)	0.0233(6)	0.0081(10)

were reproduced in three additional experimental runs, each involving two or more crystals. In one run, forsterite III remained crystalline on decompression until at least 12 GPa, but became amorphous at ambient pressure.

Lattice parameter and volume compression data for Mg_2SiO_4 are shown in Figures 3 and 4 and Table 2. The volume-pressure data to 48 GPa were fit with a third-order Birch-Murnaghan equation of state (Fig. 3). Using the measured ambient-pressure unit-cell volume (V_0) of 290.1(1) $Å^3$ and fixing the ambient-pressure isothermal bulk modulus (K_{0T}) at 127.5 GPa, we obtain a value of 4.31(1) for the first pressure-derivative of the bulk modulus (K'_{0T}). The ambient-pressure adiabatic bulk modulus of forsterite has been well characterized from ultrasonic, resonance, and Brillouin measurements and has a mean value of 128.8(5) GPa (Zha et al. 1996; Isaak 2001). The corresponding isothermal bulk modulus is 127.5 GPa, obtained using $K_{0T} = K_{0S}/(1 + \alpha\gamma_{th}T)$, where α is the thermal expansivity, γ_{th} is the thermal Gruneisen parameter, and T is temperature. Values for α and γ_{th} are from Anderson and Isaak (1995).

If both K_{0T} and K'_{0T} are allowed to vary, the resultant fit parameters are: $K_{0T} = 130.0(9)$ GPa and $K'_{0T} = 4.12(7)$. If the Vinet equation of state (Vinet et al. 1989) is used for fitting instead, the results are: $K_{0T} = 129(1)$ GPa and $K'_{0T} = 4.33(8)$. K'_{0T} values from previous static compression studies (Kudoh and Takeuchi 1985; Will et al. 1986; Andrault et al. 1995; Downs et al. 1996; Zhang 1998) range from 4.0–4.3, whereas a Brillouin scattering study to 16.2 GPa (Zha et al. 1996) resulted in $K'_{0T} = 4.2(2)$ (Table 3). Values for the pressure-derivative of the bulk modulus, as reported in previous theoretical studies of forsterite using density functional theory, range from 4.0–4.3 (da Silva et al. 1997; Li et al. 2007; Ottonello et al. 2009). Within uncertainty, K'_{0T} values from all three of these different techniques (computation, X-ray diffraction, Brillouin scattering) are in good agreement with each other and with our results.
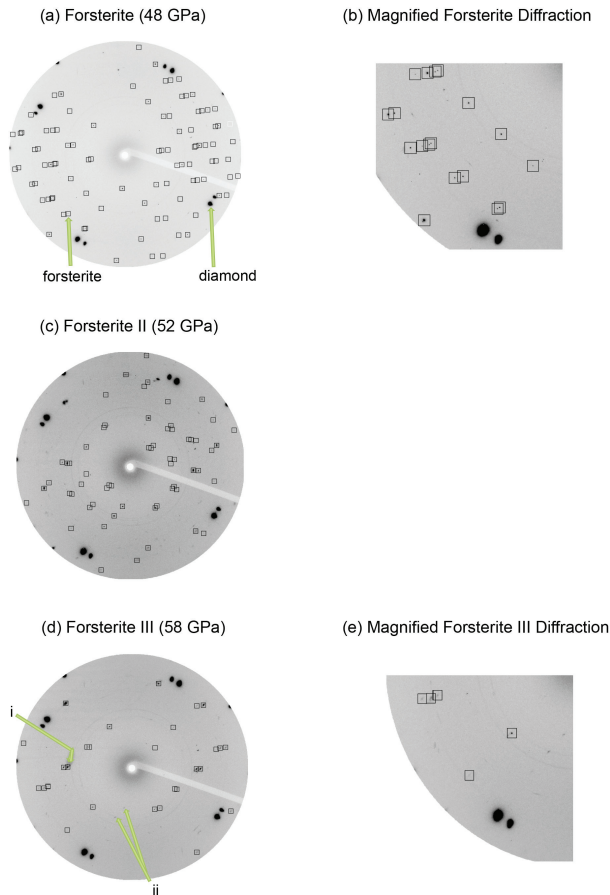
FIGURE 2. (**a**) Diffraction pattern at 48 GPa. Boxes are shown around forsterite diffraction peaks that were used in the analysis. (**b**) Expanded image of forsterite diffraction peaks in **a**. (**c**) Diffraction pattern at 52 GPa. Indexed peaks for forsterite II are shown from two different twin domains. (**d**) Diffraction pattern of forsterite III at 58 GPa. The arrows (i and ii) show peaks that may be due to residual domains of forsterite II. (**e**) Expanded image of forsterite III diffraction peaks from **d**. Diffuse scattering results in distorted shapes for some peaks.

FIGURE 3. Unit-cell volume of forsterite from this study (filled symbols) compared to previous powder diffraction experiments (open symbols). The shaded region shows the range over which we observe forsterite II. Where not shown for filled symbols, error bars are smaller than the symbol size.

FIGURE 4. Relative axial lengths of forsterite compared with selected previous studies. Circles, diamonds, and squares are lattice parameters *a*, *b*, and *c*, respectively. Dashed lines show the fits to the axial compression data.

For the individual lattice parameters, we find that the most to least compressible axes are, in order, $b > c > a$, in agreement with previous studies on forsterite. Axial compression data were fit to a modified third-order Birch-Murnaghan equation (Xia et al. 1998). The compression behavior of the lattice parameters is similar to that reported in previous single-crystal studies (Downs et al. 1996; Zha et al. 1998), and varies smoothly up to the phase transition pressure (Fig. 4). Linear compressibilities were calculated from fits to the axial compressibility data and are in good agreement with values constrained independently from measurements of elastic constants (Isaak et al. 1989; Zha et al. 1996) (Fig. 5).

In comparison with a previous powder X-ray diffraction study by Andrault et al. (1995), our results show significant differences in the *a* and *b* parameters at high pressures (Fig. 4). At 40–50 GPa, Andrault et al. noted a change in the slope of all three of the lattice parameters and proposed a change in the compression mechanism of forsterite. In addition, they note the appearance of a
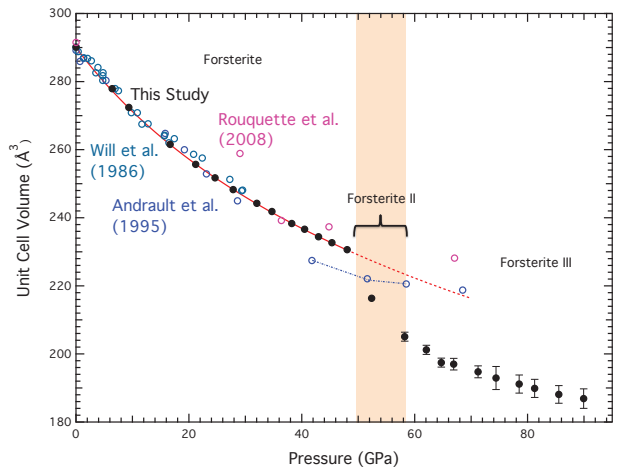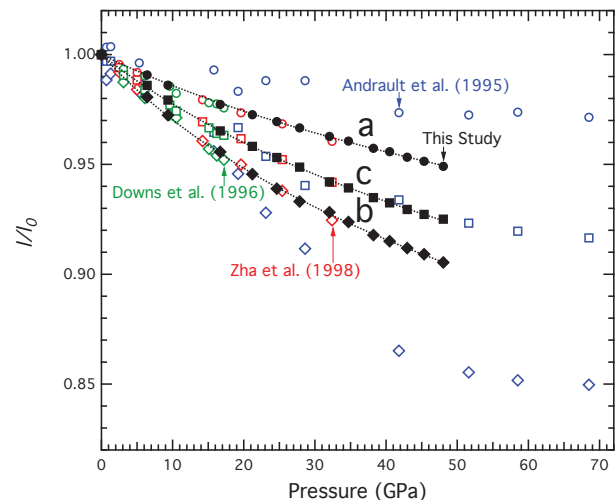
small number of new diffraction peaks at ~35 GPa, and conclude that these peaks are the result of the partial transformation of olivine to a spinel-like structure. They hypothesize that this transition is not completed due to slow kinetics compared with pressure-induced amorphization, which they propose is the main process of structural reorganization in forsterite at high pressure and 300 K.

In a non-hydrostatic Raman spectroscopic study to 50 GPa (Durben et al. 1993), two new Raman bands were observed above 30 GPa. These were interpreted as being related to a defective olivine structure in which adjacent SiO_4 polyhedra polymerized upon compression as a predecessor to pressure-induced amorphization. Additional non-hydrostatic powder X-ray and Mössbauer data on an Fe-bearing olivine (Rouquette et al. 2008) are also consistent with the lattice parameter and unit-cell volume trends seen by Andrault et al.

TABLE 2. Mg_2SiO_4 lattice parameters and unit-cell volume

Au a (Å)	P (GPa)	a (Å)	b (Å)	c (Å)	V (Å³)
		Forsterite			
	0	4.7543(5)	10.201(2)	5.9819(8)	290.1(1)
4.0317	6.4	4.7102(5)	10.004(5)	5.898(1)	277.9(2)
4.0130	9.4	4.6881(5)	9.920(4)	5.8581(6)	272.4(2)
3.9720	16.7	4.6465(4)	9.749(4)	5.7740(6)	261.6(2)
3.9499	21.2	4.6242(5)	9.646(4)	5.7320(6)	255.7(2)
3.9343	24.6	4.6092(5)	9.579(4)	5.7016(6)	251.7(2)
3.9206	27.8	4.5956(6)	9.519(5)	5.6755(7)	248.3(2)
3.9038	32.0	4.5772(5)	9.469(4)	5.6352(6)	244.2(2)
3.8937	34.7	4.5671(4)	9.424(4)	5.6190(6)	241.8(2)
3.8809	38.2	4.5514(4)	9.363(4)	5.5924(6)	238.3(2)
3.8730	40.5	4.5441(5)	9.335(4)	5.5782(6)	236.6(2)
3.8647	43.0	4.5320(5)	9.303(5)	5.5603(7)	234.4(2)
3.8569	45.3	4.5232(5)	9.274(5)	5.5467(7)	232.7(2)
3.8484	48.0	4.5125(5)	9.236(5)	5.5337(7)	230.6(2)
		Forsterite II			
Au a (Å)	P (GPa)	a (Å), α (°)	b (Å), β (°)	c (Å), γ (°)	V (Å³)
3.8353	52.4	4.683(2), 93.0(2)	9.21(3), 106.94(5)	5.317(6), 97.8(1)	216.4(7)
		Forsterite III			
Au a (Å)	P (GPa)	a (Å)	b (Å)	c (Å)	V (Å³)
3.8186	58.2	2.640(2)	8.596(8)	9.04(4)	205(1)
3.8082	62.1	2.630(2)	8.566(9)	8.93(4)	201(1)
3.8013	64.7	2.623(2)	8.554(9)	8.80(4)	197(1)
3.7957	66.9	2.622(2)	8.55(1)	8.79(6)	197(2)
3.7850	71.2	2.612(2)	8.52(1)	8.76(6)	195(2)
3.7774	74.4	2.606(3)	8.49(2)	8.7(1)	193(3)
3.7679	78.5	2.597(3)	8.45(2)	8.71(9)	191(3)
3.7618	81.2	2.591(3)	8.43(2)	8.70(9)	190(3)
3.7525	85.5	2.584(3)	8.40(2)	8.67(9)	188(3)
3.7433	89.9	2.574(3)	8.37(2)	8.7(1)	187(3)

Note: Numbers in parentheses represent one standard deviation uncertainty in the last digit.

In this work, we observe no changes in the forsterite diffraction pattern or compression trends to 48 GPa and no evidence for amorphization. These differences may reflect the role of non-hydrostatic stresses in the previous experiments. However, interpretation of the earlier powder diffraction experiments is hindered by their poor signal-to-noise ratio and low angular resolution. The proposed change in compression mechanism from previous work may instead be transformation to the forsterite II phase near 50 GPa. It is also notable that shock compression data for Mg-rich olivine show a mixed-phase region indicating a high-pressure phase transition beginning from about 50 GPa (Brown et al. 1987).

The diffraction data for forsterite II show that it is a triclinic phase with unit-cell lengths similar to those of forsterite. At 52 GPa, the lattice parameters are $a = 4.683(2)$, $b = 9.21(3)$, $c = 5.317(6)$ Å, $\alpha = 93.0(2)$, $\beta = 106.94(5)$, and $\gamma = 97.8(1)°$. Forsterite II was observed in diffraction patterns between 50.1 and 55.2 GPa; however, a step scan was only carried out at 52.4 GPa and

so the unit cell has been determined only at this pressure (Fig. 3). The volume reduction associated with the transition is ~4.8%.

The unit cell of forsterite III was constrained from diffraction data between 58.2 and 89.9 GPa. It is a base-centered orthorhombic cell, characterized by an a-axis that is approximately one third that of b and c (Table 2). At 58.2 GPa, the lattice parameters are $a = 2.640(2)$, $b = 8.596(8)$, and $c = 9.04(4)$ Å. The c-parameter has larger uncertainty as a result of the diffuse scattering (and therefore disorder) observed in that direction. There is a clear relationship between the initial low-pressure forsterite unit cell and the unit cell of forsterite III, as the a-, b-, and c-parameters of forsterite III are, respectively, half the c-parameter, double the a-parameter, and the same as the b-parameter of forsterite.

Analysis of systematic absences places the new structure in the orthorhombic Patterson group $Cmmm$. Structure searches using USPEX and the experimental cell parameters at 58.2 GPa established the structure and its space group, $Cmc2_1$, which is an acentric subgroup of the $Cmcm$ space group. (CIF[1] on deposit.) At the experimental cell parameters, the simulations show that the model structure has a hydrostatic stress tensor consistent with the experimental pressure. This structure is confirmed by our experimental data, and we were able to perform its Rietveld refinement. Metadynamics simulations revealed a stepwise phase transition sequence consistent with our experimental findings. The transitions occur by shear deformation of forsterite in [001](100) with displacement vectors of approximately 1/4 **c** + 1/12 **b**. This results in a change in stacking sequence of the oxygen structure from hexagonal to cubic-like, and changes the Si coordination from 4 to 6. After ~600 metadynamics steps, half of the Si ions are in sixfold coordination and the structure is characterized by alternating layers of octahedral and tetrahedral Si. The volume is reduced by ~5%. Between metadynamics steps 600 and 700, the intermediate structure is further compressed by similar shear deformations, which results in a subsequent increase in the number of octahedral Si atoms, although fivefold-coordinated Si are also observed. The final structure, which is similar, but not identical, to the structure found using USPEX, has a volume that is about 10% smaller than the original forsterite and essentially all Si in an octahedral environment. These volume reductions are consistent with those observed experimentally between forsterite, forsterite II, and forsterite III. The remaining disorder on the Si sites may be due to the large

---

[1] Deposit item AM-14-103, CIFs. Deposit items are stored on the MSA web site and available via the *American Mineralogist* Table of Contents. Find the article in the table of contents at GSW (ammin.geoscienceworld.org) or MSA (www.minsocam.org), and then click on the deposit link.

TABLE 3. Comparison of equation of state data for Mg-rich olivines

Reference	Composition	Pressure medium	P_{Max} (GPa)	K_{0T} (GPa)	K'_{0T}
		Single-crystal X-ray diffraction			
This study	Mg_{100}	He	50	130.0(9)	4.12(7)
Zhang (1998)	Mg_{100}	4:1 meth-eth	10	127(4)	4.2(8)
Downs et al. (1996)	Mg_{100}	4:1 meth-eth, Ar, He	17	125(2)	4.0(4)
Kudoh and Takeuchi (1985)	Mg_{100}	4:1 meth-eth	15	122.6[a]	4.3[a]
Zha et al. (1998)	Mg_{90}	Ne	32	128(2)	3.8(2)
		Polycrystalline X-ray diffraction			
Andrault et al. (1995)	Mg_{100}	none	42	128(8)	4.0[b]
Will et al. (1986)	Mg_{100}	4:1 meth-eth	30	136(1)	4.0(1)
		Brillouin spectroscopy			
Zha et al. (1996)	Mg_{100}	4:1 meth-eth, Ar, He	16	128.8(5)	4.2(2)

[a] Uncertainty not provided.
[b] Fixed value.

shear stresses involved in metadynamics and incomplete annealing. In addition, there are some stacking faults, but those could be equally present in the experiment, as indicated by the observed diffuse scattering in the diffraction patterns of the high-pressure forsterite structures. For the comparison between metadynamics and experiment, it should be kept in mind that shear deformation in real samples should involve dislocations that are not modeled here. The small system size only allows for homogeneous shear, which requires unrealistic shear stresses. However, with metadynamics easy shear planes are readily identified, which makes the proposed mechanism to the post-spinel phase a plausible one.

A candidate structure for forsterite II was also extracted from the metadynamics simulations. The repeat unit of the structure obtained after ~600 metadynamics steps contained 112 atoms and
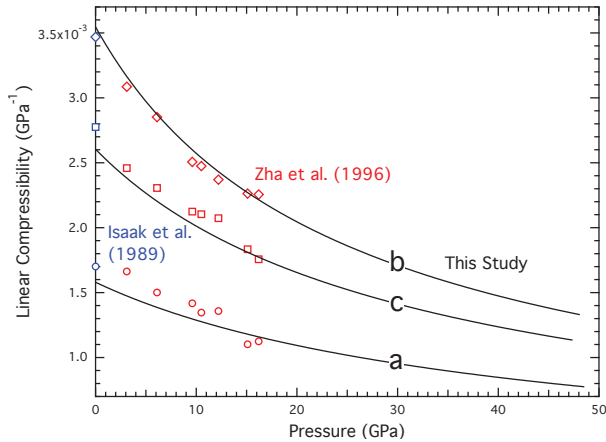

FIGURE 5. Linear compressibilities along the unit-cell axes for forsterite (solid lines) compared with measured values from single-crystal elastic constants (open symbols).

TABLE 4. Atomic parameters of forsterite II at 52.4 GPa optimized using DFT ($a = 4.695$, $b = 9.201$, $c = 5.311$ Å, $\alpha = 93.100$, $\beta = 107.264$, $\gamma = 98.133°$)

Atom	Wyckoff position	x/a	y/b	z/c	Coordination
Mg1	1a	0.9714	0.0966	0.6415	7
Mg2	1a	0.0419	0.9354	0.0567	7
Mg3	1a	0.0026	0.6656	0.7362	6
Mg4	1a	0.5065	0.5160	0.8488	6
Mg5	1a	0.5386	0.7905	0.1388	6
Mg6	1a	0.0105	0.3666	0.9614	6
Mg7	1a	0.4746	0.2414	0.5588	6
Mg8	1a	0.5065	0.5161	0.3489	6
Si1	1a	0.0048	0.3875	0.4564	6
Si2	1a	0.0083	0.6445	0.2412	6
Si3	1a	0.6136	0.1239	0.0951	4
Si4	1a	0.3995	0.9081	0.6027	4
O1	1a	0.2702	0.8430	0.8193	
O2	1a	0.7865	0.6995	0.9680	
O3	1a	0.7628	0.2287	0.3717	
O4	1a	0.2756	0.0474	0.4928	
O5	1a	0.7429	0.1891	0.8786	
O6	1a	0.2266	0.3325	0.7297	
O7	1a	0.2506	0.8032	0.3262	
O8	1a	0.7833	0.6947	0.4029	
O9	1a	0.7924	0.4622	0.1735	
O10	1a	0.7372	0.9845	0.2048	
O11	1a	0.2204	0.5698	0.5243	
O12	1a	0.7760	0.4475	0.6450	
O13	1a	0.2685	0.1109	0.0031	
O14	1a	0.2370	0.5847	0.0528	
O15	1a	0.2300	0.3374	0.2947	
O16	1a	0.7446	0.9211	0.6950	

Si in both tetrahedral and octahedral coordination. Closer inspection suggested the presence of (100) stacking faults. After their removal, a $P1$ triclinic unit cell with 28 atoms and lattice parameters similar to the experimental ones was extracted (Table 4 and Fig. 6). Structure refinements from the experimental data were not possible due to extensive twinning of the crystal as well as the low peak-to-parameter ratio in the refinement. The DFT refined lattice parameters at 52.4 GPa are $a = 4.695$, $b = 9.201$, $c = 5.311$ Å, $\alpha = 93.100$, $\beta = 107.264$, and $\gamma = 98.133°$, which are consistent with the experimental values reported above. The atomic positions are given in Table 4. This structure consists of a framework of edge-sharing Mg polyhedra, one-quarter of which are 7-coordinated in a distorted pentagonal bipyramid configuration, and three-quarters of which are octahedrally coordinated. Half of the Si is octahedrally coordinated, and half is tetrahedrally coordinated. Each of two edge-sharing Si octahedra shares a corner with a Si tetrahedron to form isolated four-membered Si polyhedral chains (tetrahedron-octahedron-octahedron-tetrahedron) that are kinked between the tetrahedra and octahedra. When viewed along [001], the structure consists of layers of Mg and Si octahedra alternating with layers of
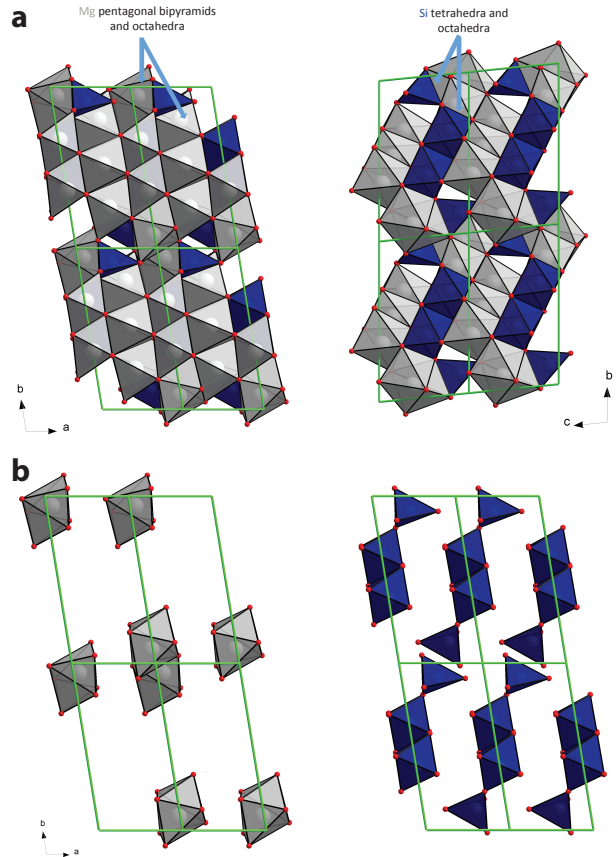

FIGURE 6. (**a**) A model of the forsterite II structure derived from metadynamics and optimized using DFT calculations. Gray polyhedra represent Mg sites and blue polyhedra Si sites. Oxygen ions are red. Si ions are located in both octahedral and tetrahedral sites, and Mg ions are located in both octahedral and pentagonal bipyramidal sites. (**b**) The Mg pentagonal bipyramids in forsterite II. (**c**) The Si tetrahedral and octahedral chains in forsterite II.

Si tetrahedra and Mg pentagonal bipyramids (Fig. 6).

AB$_2$O$_4$ compounds commonly adopt the spinel structure. High-pressure transformations in oxide spinels can involve various disproportionation pathways (perovskite + oxide, rutile + oxide, ilmenite + oxide), formation of a distorted spinel (Greenberg et al. 2011), or transformation to one of several post-spinel structures such as calcium ferrite and related structures (CaFe$_2$O$_4$, CaTi$_2$O$_4$, CaMn$_2$O$_4$) (Reid and Ringwood 1969; Andrault and Bolfan-Casanova 2001; Chen et al. 2003; Dubrovinsky et al. 2003; Yamanaka et al. 2008). The CaFe$_2$O$_4$-type phase is believed to be an important host for aluminum in subducted basaltic oceanic crust (Ono et al. 2002). On the basis of lattice parameter ratios alone, a post-spinel structure could be identified as a possible candidate for forsterite III, and this was confirmed by the structure solution calculations. Thus, under room-temperature compression, forsterite transforms via a triclinic intermediate structure (forsterite II) over a narrow pressure range to a post-spinel structure, in sharp contrast to its high-temperature transformation sequence from olivine to spinelloid to spinel to perovskite and oxide. However, it should be noted that DFT calculations show forsterite II and III to be energetically metastable when compared with their high-temperature counterparts.

Post-spinel phases are characterized by chains of edge- and corner-sharing octahedra with channels that run parallel to the c-axis. Changes in octahedral linkage and site distortion differentiate the individual members in this family. Depending on the cation and anion sizes, the ions that reside in the channels can have different coordination. The most frequently observed post-spinel structures are the CaMn$_2$O$_4$-, CaFe$_2$O$_4$-, and CaTi$_2$O$_4$-type structures (Yamanaka et al. 2008), but for forsterite III, the most energetically (meta)stable structure is a non-centrosymmetric version of the Cmcm CaTi$_2$O$_4$-type structure, in which half of the Mg ions (Mg2 site) reside in the face-sharing trigonal prismatic site (the c-axis-aligned channels), while the other half of the Mg ions (Mg1 site) share the octahedral Ti site with the Si ions (Fig. 7). This arrangement is analogous to an inverse spinel, since the larger cation, Mg^{2+}, occupies both the larger trigonal prismatic site and the smaller octahedral site.

Since we only have a limited number of observed unique diffraction peaks (24 at 58.2 GPa) compared with the number of refinable parameters in the proposed forsterite III structure (1 free variable, 14 positional parameters, and 7 isotropic thermal displacement parameters), we refined the structure by alternating refinements between the cations and anions until the refinement was nearly complete. At that point we fixed the isotropic thermal displacement parameters, and refined all the atomic position coordinates together. The refined structure is similar to the structure proposed by theory, but with more distorted coordination polyhedra (see Table 5 for atomic coordinates from experiment and theory and Fig. 7 for a visual comparison). The most sig-
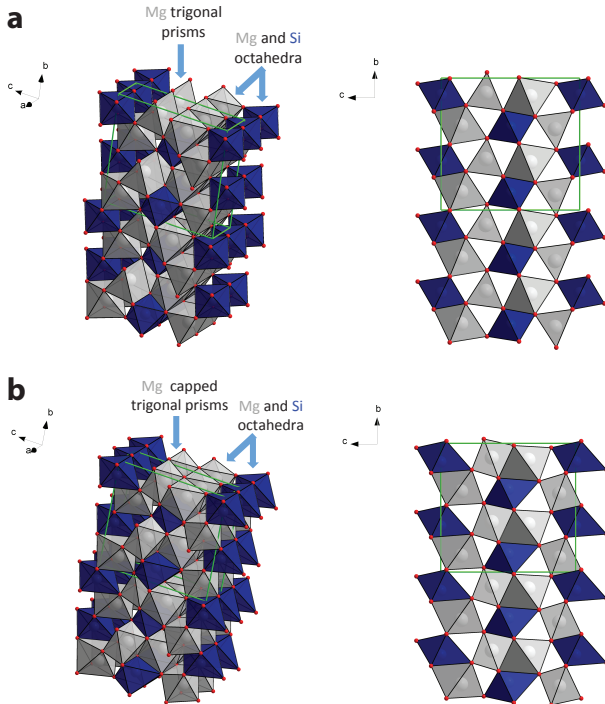

FIGURE 7. (a) A model of the forsterite III structure optimized using DFT. Gray polyhedra represent Mg sites and blue polyhedra Si sites. Oxygen atoms are red. Si atoms are located in octahedral sites, and Mg atoms are located in both octahedral and face-sharing trigonal prism sites. **(b)** A model of the forsterite III structure refined against experimental single-crystal diffraction intensities. Mg atoms have shifted position compared with the theoretical model such that half of them are now in a 7-coordinated capped trigonal prism site.

TABLE 5a. Representative single-crystal structure refinement for forsterite III at 58.2 GPa

Beamline	16 ID-B, HPCAT, APS, ANL
Wavelength (Å)	0.39891
Pressure (GPa)	58.2
Temperature (K)	298
Composition	Mg$_2$SiO$_4$
Symmetry	Orthorhombic, Cmc2$_1$
Lattice Parameters a, b, c, (Å)	2.640 (2), 8.596(8), 9.04(4)
Volume (Å^3)	205(1)
Z	4
R_{int}	0.060
Reflection range	$-2 \leq h \leq 2, -7 \leq k \leq 9, -5 \leq l \leq 3$
Maximum 2θ (°)	24.93
Number independent reflections	24
Refinement	F^2
R	0.052
wR$_2$	0.120

TABLE 5b. Refined atomic parameters for forsterite III at 58.2 GPa

Atom	Wyckoff position	x/a	y/b	z/c	U_{iso}
Mg1	4a	0.5	0.373(12)	0.350(13)	0.009(8)
Mg2	4a	0.5	0.889(5)	0.622(14)	0.012(8)
Si	4a	0	0.857(16)	0.000(15)	0.018(8)
O1	4a	0.5	0.983(60)	0.46(15)	0.022(14)
O2	4a	0.5	0.231(14)	0.572(55)	0.004(12)
O3	4a	0.5	0.706(14)	0.271(44)	0.023(25)
O4	4a	0.5	0.466(16)	0.181(91)	0.011(14)

TABLE 5c. Atomic parameters of forsterite III at 58.2 GPa optimized using DFT (a = 2.591, b = 8.726, c = 8.794 Å)

Atom	Wyckoff position	x/a	y/b	z/c
Mg1	4a	0.5	0.3636	0.3541
Mg2	4a	0.5	0.8861	0.6777
Si	4a	0	0.8720	0.0000
O1	4a	0.5	0.00466	0.4406
O2	4a	0.5	0.2537	0.5490
O3	4a	0.5	0.7048	0.3247
O4	4a	0.5	0.4526	0.1647

nificant difference is that for the M2 site, the Mg ions move far enough away from the centers of the trigonal prisms that they become 7-coordinated in a capped trigonal prism configuration. However, this refinement should be considered preliminary due to the low peak-to-parameter ratio.

While the uncertainty in the unit-cell parameters is relatively large for the high-pressure phase, there is clearly a substantial volume decrease associated with the phase transition sequence. The volume of forsterite III is ~9% lower than the extrapolated volume of forsterite I, consistent with the metadynamics calculations. For comparison, the volume difference between forsterite and the high *P-T* polymorphs wadsleyite and ringwoodite are 7.6 and 10.4%, respectively, at ambient conditions.

In summary, our combined experimental data and theoretical calculations have revealed the existence of new metastable phases of forsterite above 50 GPa under room-temperature compression, in contrast with earlier reports of a change in compression mechanism and amorphization. Metastable olivine polymorphs are potentially important for understanding phases formed in laboratory shock experiments as well as those found naturally in meteorites and impact sites (Van de Moortèle et al. 2007). Future work should focus on the effect of iron on high-pressure behavior in this system. In addition, single-crystal diffraction studies on forsterite to higher pressures as well as combined high pressure-temperature conditions are needed.

References Cited

Adjaoud, O., Steinle-Neumann, G., and Jahn, S. (2011) Transport properties of Mg_2SiO_4 liquid at high pressure: Physical state of a magma ocean. Earth and Planetary Science Letters, 312, 463–470.

Adjaoud, O., Marquardt, K., and Jahn, S. (2012) Atomic structures and energies of grain boundaries in Mg_2SiO_4 forsterite from atomistic modeling. Physics and Chemistry of Minerals, 39, 749–760.

Anderson, O.L., and Isaak, D.G. (1995) Elastic constants of mantle minerals at high temperature. In T.J. Ahrens, Ed., Mineral Physics & Crystallography: A Handbook of Physical Constants, AGU Reference Shelf, 2, p. 64–97. AGU, Washington, D.C.

Andrault, D., and Bolfan-Casanova, N. (2001) High-pressure phase transformations in the $MgFe_2O_4$ and Fe_2O_3–$MgSiO_3$ systems. Physics and Chemistry of Minerals, 28, 211–217.

Andrault, D., Bouhifd, M.A., Itié, J.P., and Richet, P. (1995) Compression and amorphization of (Mg,Fe)₂SiO₄ olivines: An X-ray diffraction study up to 70 GPa. Physics and Chemistry of Minerals, 22, 99–107.

Angel, R.J., Bujak, M., Zhao, J., Gatta, G.D., and Jacobsen, S.D. (2007) Effective hydrostatic limits of pressure media for high-pressure crystallographic studies. Journal of Applied Crystallography, 40, 26–32.

Birle, J.D., Gibbs, G.V., Moore, P.B., and Smith, J.V. (1968) Crystal structures of natural olivines. American Mineralogist, 53, 807–824.

Bragg, W.L., and Brown, G.B. (1926) Die struktur des olivins. Zeitschrift für Kristallographie, 63, 538–556.

Brown, J.M., Furnish, M.D., and McQueen, R.G. (1987) Thermodynamics for (Mg,Fe)₂SiO₄ from the Hugoniot. In M. Manghnani and Y. Syono, Eds., High Pressure Research in Mineral Physics, p. 373–384. AGU, Washington, D.C.

Catlow, C.R.A. (1977) Point defect and electronic properties of uranium dioxide. Proceedings of the Royal Society of London. A. Mathematical and Physical Sciences, 353, 533–561.

Chen, M., Shu, J., Mao, H.K., Xie, X., and Hemley, R.J. (2003) Natural occurrence and synthesis of two new postspinel polymorphs of chromite. Proceedings of the National Academy of Sciences, 100, 14651–14654.

Crovisier, J., Leech, K., Bockelée-Morvan, D., Brooke, T.Y., Hanner, M.S., Altieri, B., Keller, H.U., and Lellouch, E. (1997) The spectrum of comet Hale-Bopp (C/1995 O1) observed with the Infrared Space Observatory at 2.9 astronomical units from the Sun. Science, 275, 1904–1907.

da Silva, C., Stixrude, L., and Wentzcovitch, R.M. (1997) Elastic constants and anisotropy of forsterite at high pressure. Geophysical Research Letters, 24, 1963–1966.

de Koker, N.P., Stixrude, L., and Karki, B.B. (2008) Thermodynamics, structure, dynamics, and freezing of Mg_2SiO_4 liquid at high pressure. Geochimica et Cosmochimica Acta, 72, 1427–1441.

Deer, W.A., Howie, R.A., and Zussman, J. (1982) Orthosilicates. Longman, London.

Dera, P., Lavina, B., Borkowski, L.A., Prakapenka, V.B., Sutton, S.R., Rivers, M.L., Downs, R.T., Boctor, N.Z., and Prewitt, C.T. (2009) Structure and behavior of the barringerite Ni end-member, Ni_2P, at deep Earth conditions and implications for natural Fe-Ni phosphides in planetary cores. Journal of Geophysical Research, 114(B3), B03201.

Dera, P., Lazarz, J.D., and Lavina, B. (2011a) Pressure-induced development of bonding in NiAs type compounds and polymorphism of NiP. Journal of Solid State Chemistry, 184, 1997–2003.

Dera, P., Lazarz, J.D., Prakapenka, V.B., Barkley, M., and Downs, R.T. (2011b) New insights into the high-pressure polymorphism of SiO_2 cristobalite. Physics and Chemistry of Minerals, 38, 1–13.

Downs, R.T., Zha, C.S., Duffy, T.S., and Finger, L.W. (1996) The equation of state of forsterite to 17.2 GPa and effects of pressure media. American Mineralogist, 81, 51–55.

Dubrovinsky, L.S., Dubrovinskaia, N.A., McCammon, C., Rozenberg, G.K., Ahuja, R., Osorio-Guillen, J.M., Dmitriev, V., Weber, H.P., Bihan, T.L., and Johansson, B. (2003) The structure of the metallic high-pressure Fe_3O_4 polymorph: Experimental and theoretical study. Journal of Physics: Condensed Matter, 15, 7697–7706.

Dubrovinsky, L., Boffa-Ballaran, T., Glazyrin, K., Kurnosov, A., Frost, D., Merlini, M., Hanfland, M., Prakapenka, V.B., Schouwink, P., and Pippinger, T. (2010) Single-crystal X-ray diffraction at megabar pressures and temperatures of thousands of degrees. High Pressure Research, 30, 620–633.

Durben, D.J., McMillan, P.F., and Wolf, G.H. (1993) Raman study of the high-pressure behavior of forsterite (Mg_2SiO_4) crystal and glass. American Mineralogist, 78, 1143–1148.

Fei, Y., Ricolleau, A., Frank, M., Mibe, K., Shen, G., and Prakapenka, V. (2007) Toward an internally consistent pressure scale. Proceedings of the National Academy of Sciences, 104, 9182–9186.

Gale, J.D. (2005) GULP: capabilities and prospects. Zeitschrift für Kristallographie, 220, 552–554.

Glass, C.W., Oganov, A.R., and Hansen, N. (2006) USPEX—evolutionary crystal structure prediction. Computer Physics Communications, 175, 713–720.

Gonze, X., Amadon, B., Anglade, P.M., Beuken, J.M., Bottin, F., Boulanger, P., Bruneval, F., Caliste, D., Caracas, R., and Cote, M. (2009) ABINIT: First-principles approach to material and nanosystem properties. Computer Physics Communications, 180, 2582–2615.

Greenberg, E., Dubrovinsky, L.S., McCammon, C., Rouquette, J., Kantor, I., Prakapenka, V., Rozenberg, G.K., and Pasternak, M.P. (2011) Pressure-induced structural phase transition of the iron end-member of ringwoodite (γ-Fe_2SiO_4) investigated by X-ray diffraction and Mössbauer spectroscopy. American Mineralogist, 96, 833–840.

Gurmani, S.F., Jahn, S., Brasse, H., and Schilling, F.R. (2011) Atomic scale view on partially molten rocks: Molecular dynamics simulations of melt-wetted olivine grain boundaries. Journal of Geophysical Research, 116, B12209.

Guyot, F., and Reynard, B. (1992) Pressure-induced structural modifications and amorphization in olivine compounds. Chemical Geology, 96, 411–420.

Haigis, V., Salanne, M., and Jahn, S. (2012) Thermal conductivity of MgO, $MgSiO_3$ perovskite and post-perovskite in the earth's deep mantle. Earth and Planetary Science Letters, 355-356, 102–108.

Hammersley, A.P., Svensson, S.O., Hanfland, M., Fitch, A.N., and Hausermann, D. (1996) Two-dimensional detector software: From real detector to idealised image or two-theta scan. High Pressure Research, 14, 235–248.

Hazen, R.M., and Finger, L.W. (1982) Comparative Crystal Chemistry: Temperature, pressure, composition, and the variation of crystal structure, 250 p. Wiley, New York.

Isaak, D.G. (2001) Elastic properties of minerals and planetary objects. In M. Levy, J.D. Bass, and R. Stern, Eds., Handbook of Elastic Properties of Solids, Liquids, and Gases: Volume III: Elastic Properties of Solids: Biological and Organic Material, Earth and Marine Sciences, p. 325–376. Academic Press, San Diego.

Isaak, D.G., Anderson, O.L., and Goto, T. (1989) Elasticity of single-crystal forsterite measured to 1700 K. Journal of Geophysical Research, 94(B5), 5895–5906.

Jahn, S., and Madden, P.A. (2007) Modeling Earth materials from crustal to lower mantle conditions: A transferable set of interaction potentials for the CMAS

system. Physics of the Earth and Planetary Interiors, 162, 129–139.

Jahn, S., and Martoňák, R. (2008) Plastic deformation of orthoenstatite and the ortho-to high-pressure clinoenstatite transition: A metadynamics simulation study. Physics and Chemistry of Minerals, 35, 17–23.

Kantor, A., Kantor, I., Merlini, M., Glazyrin, K., Prescher, C., Hanfland, M., and Dubrovinsky, L. (2012) High-pressure structural studies of eskolaite by means of single-crystal X-ray diffraction. American Mineralogist, 97, 1764–1770.

Karato, S., and Wu, P. (1993) Rheology of the upper mantle: A synthesis. Science, 260, 771–778.

Kawakatsu, H., and Yoshioka, S. (2011) Metastable olivine wedge and deep dry cold slab beneath southwest Japan. Earth and Planetary Science Letters, 303, 1–10.

Kirby, S.H., Stein, S., Okal, E.A., and Rubie, D.C. (1996) Metastable mantle phase transformations and deep earthquakes in subducting oceanic lithosphere. Reviews of Geophysics, 34, 261–306.

Kudoh, Y., and Takeuchi, Y. (1985) The crystal structure of forsterite Mg_2SiO_4 under high pressure up to 149 kb. Zeitschrift für Kristallographie, 171, 291–302.

Lavina, B., Dera, P., Kim, E., Meng, Y., Downs, R.T., Weck, P.F., Sutton, S.R., and Zhao, Y. (2011) Discovery of the recoverable high-pressure iron oxide Fe_4O_5. Proceedings of the National Academy of Sciences, 108, 17281–17285.

Lavina, B., Dera, P.K., Downs, R.T., Yang, W., Sinogeikin, S.V., Meng, Y., Shen, G., and Schiferl, D. (2010) Structure of siderite $FeCO_3$ to 56 GPa and hysteresis of its spin-pairing transition. Physical Review B, 82, 064110.

Lewis, G.V., and Catlow, C.R.A. (1985) Potential models for ionic oxides. Journal of Physics C: Solid State Physics, 18, 1149–1161.

Li, L., Wentzcovitch, R.M., Weidner, D.J., and Da Silva, C.R.S. (2007) Vibrational and thermodynamic properties of forsterite at mantle conditions. Journal of Geophysical Research, 112, B05206.

Lyakhov, A.O., Oganov, A.R., and Valle, M. (2010) How to predict very large and complex crystal structures. Computer Physics Communications, 181, 1623–1632.

Lyakhov, A.O., Oganov, A.R., Stokes, H.T., and Zhu, Q. (2013) New developments in evolutionary structure prediction algorithm USPEX. Computer Physics Communications, 184, 1172–1182.

Ma, Y., Eremets, M., Oganov, A.R., Xie, Y., Trojan, I., Medvedev, S., Lyakhov, A.O., Valle, M., and Prakapenka, V. (2009) Transparent dense sodium. Nature, 458, 182–185.

Martoňák, R., Donadio, D., Oganov, A.R., and Parrinello, M. (2006) Crystal structure transformations in SiO_2 from classical and ab initio metadynamics. Nature Materials, 5, 623–626.

Martyna, G.J., Tobias, D.J., and Klein, M.L. (1994) Constant pressure molecular dynamics algorithms. The Journal of Chemical Physics, 101, 4177–4189.

Mason, B. (1963) Olivine composition in chondrites. Geochimica et Cosmochimica Acta, 27, 1011–1023.

Merlini, M., Crichton, W.A., Hanfland, M., Gemmi, M., Müller, H., Kupenko, I., and Dubrovinsky, L. (2012) Structures of dolomite at ultrahigh pressure and their influence on the deep carbon cycle. Proceedings of the National Academy of Sciences, 109, 13509–13514.

Miletich, R., Allan, D.R., and Kuhs, W.F. (2000) High-pressure single-crystal techniques. In R.M. Hazen and R.T. Downs, Eds., High-Temperature and High-Pressure Crystal Chemistry, 41, 445–519. Reviews in Mineralogy and Geochemistry, Mineralogical Society of America, Chantilly, Virginia.

Mustard, J.F., Poulet, F., Gendrin, A., Bibring, J.P., Langevin, Y., Gondet, B., Mangold, N., Bellucci, G., and Altieri, F. (2005) Olivine and pyroxene diversity in the crust of Mars. Science, 307, 1594–1597.

Nguyen, A.N., and Zinner, E. (2004) Discovery of ancient silicate stardust in a meteorite. Science, 303, 1496–1499.

Oganov, A.R., and Glass, C.W. (2006) Crystal structure prediction using ab initio evolutionary techniques: Principles and applications. The Journal of Chemical Physics, 124, 244704.

Oganov, A.R., Glass, C.W., and Ono, S. (2006) High-pressure phases of $CaCO_3$: Crystal structure prediction and experiment. Earth and Planetary Science Letters, 241, 95–103.

Oganov, A.R., Chen, J., Gatti, C., Ma, Y., Glass, C.W., Liu, Z., Yu, T., Kurakevych, O.O., and Solozhenko, V.L. (2009) Ionic high-pressure form of elemental boron. Nature, 457, 863–867.

Oganov, A.R., Ma, Y., Lyakhov, A.O., Valle, M., and Gatti, C. (2010) Evolutionary crystal structure prediction as a method for the discovery of minerals and materials. In R. Wentzcovitch and L. Stixrude, Eds., Theoretical and Computational Methods in Mineral Physics: Geophysical Applications, 71, 271–298. Reviews in Mineralogy and Geochemistry, Mineralogical Society of America, Chantilly, Virginia.

Oganov, A.R., Lyakhov, A.O., and Valle, M. (2011) How evolutionary crystal structure prediction works and why. Accounts of Chemical Research, 44, 227–237.

Ono, S., Hirose, K., Kikegawa, T., and Saito, Y. (2002) The compressibility of a natural composition calcium ferrite-type aluminous phase to 70 GPa. Physics of the Earth and Planetary Interiors, 131, 311–318.

Ottonello, G., Civalleri, B., Ganguly, J., Vetuschi Zuccolini, M., and Noel, Y. (2009) Thermophysical properties of the α-β-γ polymorphs of Mg_2SiO_4: A computational study. Physics and Chemistry of Minerals, 36, 87–106.

Perdew, J.P., Burke, K., and Ernzerhof, M. (1996) Generalized gradient approximation made simple. Physical Review Letters, 77, 3865–3868.

Rappe, A.M., Rabe, K.M., Kaxiras, E., and Joannopoulos, J.D. (1990) Optimized pseudopotentials. Physical Review B, 41, 1227–1230.

Reid, A.F., and Ringwood, A.E. (1969) Newly observed high pressure transformations in Mn_3O_4, $CaAl_2O_4$, and $ZrSiO_4$. Earth and Planetary Science Letters, 6, 205–208.

Ringwood, A.E. (1991) Phase transformations and their bearing on the constitution and dynamics of the mantle. Geochimica et Cosmochimica Acta, 55, 2083–2110.

Rouquette, J., Kantor, I., McCammon, C.A., Dmitriev, V., and Dubrovinsky, L.S. (2008) High-pressure studies of $(Mg_{0.9}Fe_{0.1})_2SiO_4$ olivine using Raman spectroscopy, X-ray diffraction, and Mössbauer spectroscopy, Inorganic Chemistry, 47, 2668–2673.

Sanders, M.J., Leslie, M., and Catlow, C.R.A. (1984) Interatomic potentials for SiO_2. Journal of the Chemical Society, Chemical Communications, 1271–1273.

Sheldrick, G.M. (2008) A short history of SHELX. Acta Crystallographica, A64, 112–122.

Smyth, J.R., and McCormick, T.C. (1995) Crystallographic data for minerals. In T.J. Ahrens, Ed., Mineral Physics and Crystallography: A Handbook of Physical Constants, 2, 1–17. AGU, Washington, D.C.

Smyth, J.R., Jacobsen, S.D., and Hazen, R.M. (2000) Comparative crystal chemistry of orthosilicate minerals. In R.M. Hazen and R.T. Downs, Eds., High-Temperature and High-Pressure Crystal Chemistry, 41, 187–209. Reviews in Mineralogy and Geochemistry, Mineralogical Society of America, Chantilly, Virginia.

Takemura, K., and Dewaele, A. (2008) Isothermal equation of state for gold with a He-pressure medium. Physical Review B, 78, 104119.

van Boekel, R., Min, M., Leinert, C., Waters, L.B.F.M., Richichi, A., Chesneau, O., Dominik, C., Jaffe, W., Dutrey, A., Graser, U., and others. (2004) The building blocks of planets within the "terrestrial" region of protoplanetary disks. Nature, 432, 479–482.

Van de Moortèle, B., Reynard, B., McMillan, P.F., Wilson, M., Beck, P., Gillet, P., and Jahn, S. (2007) Shock-induced transformation of olivine to a new metastable $(Mg,Fe)_2SiO_4$ polymorph in Martian meteorites. Earth and Planetary Science Letters, 261, 469–475.

Vinet, P., Rose, J.H., Ferrante, J., and Smith, J.R. (1989) Universal features of the equation of state of solids. Journal of Physics: Condensed Matter, 1, 1941–1963.

Will, G., Hoffbauer, W., Hinze, E., and Lauterjung, J. (1986) The compressibility of forsterite up to 300 kbar measured with synchrotron radiation. Physica B+C, 139-140, 193–197.

Xia, X., Weidner, D.J., and Zhao, H. (1998) Equation of state of brucite; single-crystal Brillouin spectroscopy study and polycrystalline pressure-volume-temperature measurement. American Mineralogist, 83, 68–74.

Yamanaka, T., Uchida, A., and Nakamoto, Y. (2008) Structural transition of post-spinel phases $CaMn_2O_4$, $CaFe_2O_4$, and $CaTi_2O_4$ under high pressures up to 80 GPa. American Mineralogist, 93, 1874–1881.

Zha, C.S., Duffy, T.S., Downs, R.T., Mao, H.K., and Hemley, R.J. (1996) Sound velocity and elasticity of single-crystal forsterite to 16 GPa. Journal of Geophysical Research, 101, 17535–17545.

——— (1998) Brillouin scattering and X-ray diffraction of San Carlos olivine: direct pressure determination to 32 GPa. Earth and Planetary Science Letters, 159, 25–33.

Zhang, L. (1998) Single crystal hydrostatic compression of $(Mg,Mn,Fe,Co)_2SiO_4$ olivines. Physics and Chemistry of Minerals, 25, 308–312.

Zhu, Q., Oganov, A.R., Glass, C.W., and Stokes, H.T. (2012) Constrained evolutionary algorithm for structure prediction of molecular crystals: Methodology and applications. Acta Crystallographica, B68, 215–226.

Zolensky, M.E., Zega, T.J., Yano, H., Wirick, S., Westphal, A.J., Weisberg, M.K., Weber, I., Warren, J.L., Velbel, M.A., and Tsuchiyama, A. (2006) Mineralogy and petrology of comet 81P/Wild 2 nucleus samples. Science, 314, 1735–1739.